Conformal Metric Optimization on Surface (CMOS) for Deformation and Mapping in Laplace-Beltrami Embedding Space

Yonggang Shi[1], Rongjie Lai[2], Raja Gill[3], Daniel Pelletier[4], David Mohr[5], Nancy Sicotte[6], and Arthur W. Toga[1,⋆]

[1] Lab of Neuro Imaging, UCLA School of Medicine, Los Angeles, CA, USA
[2] Dept. of Mathematics, University of Southern California, Los Angeles, CA, USA
[3] Dept. of Neurology, UCLA School of Medicine, Los Angeles, CA, USA
[4] Department of Neurology, Yale School of Medicine, New Haven, CT, USA
[5] Department of Preventive Medicine, Northwestern University, Feinberg School of Medicine, Chicago, IL, USA
[6] Cedar Sinai Medical Center, Los Angeles, CA, USA

Abstract. In this paper we develop a novel technique for surface deformation and mapping in the high-dimensional Laplace-Beltrami embedding space. The key idea of our work is to realize surface deformation in the embedding space via optimization of a conformal metric on the surface. Numerical techniques are developed for computing derivatives of the eigenvalues and eigenfunctions with respect to the conformal metric, which is then applied to compute surface maps in the embedding space by minimizing an energy function. In our experiments, we demonstrate the robustness of our method by applying it to map hippocampal atrophy of multiple sclerosis patients with depression on a data set of 109 subjects. Statistically significant results have been obtained that show excellent correlation with clinical variables. A comparison with the popular SPHARM tool has also been performed to demonstrate that our method achieves more significant results.

1 Introduction

Surface mapping is an important technique in studying brain morphometry and has the potential of pinpointing atrophy in various pathologies [1]. While many methods were proposed for the modeling and mapping of anatomical surfaces [2–6], there is still a lack of general, yet feature sensitive, methods for the characterization and mapping of 3D anatomical surfaces. To overcome this challenge, one promising technique that is receiving increased interests is to use Laplace-Beltrami (LB) eigenfunctions as modeling tools of anatomical structures [7–10]. In this work, we propose a novel, and general approach for surface analysis with LB eigenfunctions by optimizing conformal metrics on surfaces.

⋆ This work was supported by NIH grants 5P41RR013642, R01-MH059708, and 5R01MH080892-03, and a DoD grant W81XWH-10-1-0882.

G. Fichtinger, A. Martel, and T. Peters (Eds.): MICCAI 2011, Part II, LNCS 6892, pp. 327–334, 2011.

The eigenfunctions of the LB operator can be considered as the extension of the Fourier basis onto 3D surfaces. The critical difference is that the LB eigenfunctions depend on surface geometry, and are invariant up to isometry. This robustness makes them ideal for intrinsic modeling of anatomical surfaces across population. For general shape classification, the LB eigenvalues were proposed as a DNA-like signature [7]. For detailed analysis of surface geometry, the eigenfunctions provide more information and have been applied to smoothing [8, 11], feature extraction [9, 12], and surface mapping [10].

The metric optimization method proposed in this work is based the embedding of surfaces into the Hilbert space l^2 with their LB eigen-systems [13]. This embedding is scale and pose invariant, and provides a general framework for intrinsic surface analysis. A histogram feature was developed for shape classification with the LB embedding [13]. One important result is that the surface is still a manifold in the embedding space and a rigorous distance measure between embedded manifolds was proposed [14]. The main contribution of this work is that we develop a general approach for surface deformation in the high-dimensional embedding space, which can be applied to various shape analysis tasks such as surface mapping. By iteratively optimizing conformal metrics on a surface, we can evolve its LB eigenvalues and eigenfunctions, and realize its deformation in the embedding space. With this novel technique, we develop an intrinsic approach for surface mapping and demonstrate its application in mapping hippocampal atrophy of multiple sclerosis (MS) patients with depression. Statistically significant results are obtained that show excellent correlation with clinical measures of depression. We also compare our method with the popular SPHARM tool [5] and demonstrate our method is able to achieve more significant mapping results.

2 Conformal Metric Optimization and LB Embedding

In this section, we introduce LB embedding with conformal metrics and develop numerical schemes with finite element methods on triangular meshes. For metric optimization, we derive the derivatives of eigenvalues and eigenfunctions with respect to the weight function in the conformal metric.

2.1 LB Embedding with Conformal Metrics

Let $(\mathcal{M}, g)$ be a genus-zero Riemannian surface where the metric g is the standard metric induced from R^3. For a function $f : \mathcal{M} \to \mathbb{R}$, the LB operator on $\mathcal{M}$ with the metric g is defined as:

$$\Delta^g_{\mathcal{M}} f = \frac{1}{\sqrt{G}} \sum_{i=1}^{2} \frac{\partial}{\partial x_i} (\sqrt{G} \sum_{j=1}^{2} g^{ij} \frac{\partial f}{\partial x_j}) \tag{1}$$

where (g^{ij}) is the inverse matrix of $g = (g_{ij})$ and $G = \det(g_{ij})$. Because the spectrum of $\Delta^g_{\mathcal{M}}$ is discrete, its eigen-system is defined as

$$\Delta^g_{\mathcal{M}} f_n = -\lambda_n f_n \quad (n = 0, 1, 2, \cdots) \tag{2}$$

where λ_n and f_n are the n-th eigenvalue and eigenfunction, respectively. Using the LB eigen-system, an embedding $I^g_{\mathcal{M}} : \mathcal{M} \to l^2$ was proposed in [13]:

$$I^g_{\mathcal{M}}(x) = (\frac{f_1(x)}{\sqrt{\lambda_1}}, \frac{f_2(x)}{\sqrt{\lambda_2}} \cdots, \frac{f_n(x)}{\sqrt{\lambda_n}}, \cdots) \quad \forall x \in \mathcal{M}. \tag{3}$$

Note that the embedding is not unique because of the sign ambiguities in the eigenfunction, i.e., both f_n and $-f_n$ are the n-th eigenfunction. For practical applications, the sign ambiguities can be resolved by anatomical priors or simply searching through all 2^N possible sign combinations when up to N eigenfunctions are used for numerical implementation.

The embedding $I^g_{\mathcal{M}}(\mathcal{M})$ is scale and pose invariant, and automatically aligns surfaces in the l^2 space for the intrinsic analysis of anatomical surfaces [14]. On the other hand, non-isometric shape differences remain intact in the embedding space and affect further analysis. As an example, we show in Fig. 1(a) and (d) two hippocampal surfaces $\mathcal{M}_1$ and $\mathcal{M}_2$ with different degree of bending. Such non-isometric shape differences lead to different eigenfunctions as shown in Fig. 1(b) and (d). Using closest point matching in the embedding space, which is approximated with the first 10 eigenfunctions in this example, we can project the mesh structure of $\mathcal{M}_1$ onto $\mathcal{M}_2$, and vice versa. The impact of non-isometric shape differences can be clearly seen in the large distortions in the projected mesh structures that are plotted in Fig. 1(c) and (f).

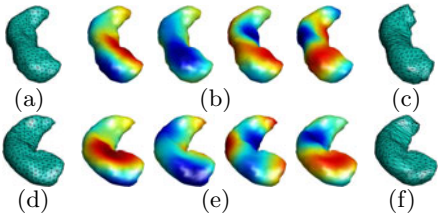

Fig. 1. Impact of non-isometric shape differences. (a)(d) Two surfaces $\mathcal{M}_1$ and $\mathcal{M}_2$. (b)(e) The 4,5,6,7-th eigenfunctions on the two surfaces. (c) (f) Projection of $\mathcal{M}_2$ onto $\mathcal{M}_1$, and $\mathcal{M}_1$ onto $\mathcal{M}_2$ with closest point matching in the embedding space.

A class of conformal metrics on $\mathcal{M}$ are denoted as $\hat{g} = \omega g$, where $\omega : \mathcal{M} \to \mathbb{R}^+$. To achieve better surface matching in the embedding space, we propose in this work to optimize the Riemannian metric in the class of metrics conformally equivalent to g. By iteratively perturbing the weight function, we can realize surface deformation in the embedding space, and minimize non-isometric shape differences. The existence of such weight functions are theoretically guaranteed since all genus-zero surfaces are conformally equivalent. Following (1), the LB operator with the conformal metric is $\Delta^{\hat{g}}_{\mathcal{M}} = \frac{1}{\omega}\Delta^g_{\mathcal{M}}$, and the eigen-system of the weighted operator is

$$\Delta^{\hat{g}}_{\mathcal{M}} f = -\lambda f. \tag{4}$$

Using the relation between $\hat{g}$ and g, we have the weak form of (4):

$$\int_{\mathcal{M}} \nabla^g_{\mathcal{M}} f \nabla^g_{\mathcal{M}} \eta d\mathcal{M} = \lambda \int_{\mathcal{M}} \omega f \eta d\mathcal{M} \quad \forall \eta : \mathcal{M} \to \mathbb{R} \tag{5}$$

where $\nabla^g_{\mathcal{M}}$ is the gradient operator on $\mathcal{M}$ with the standard metric g, and η is a test function.

For numerical computation, we represent $\mathcal{M}$ as a triangular mesh with L vertices $\mathcal{V} = \{v_i | 1 \leq i \leq L\}$. At each vertex v_i, we denote its barycentric coordinate function as ϕ_i and represent the weight function as $\omega = \sum_{j=1}^{L} \omega_j \phi_j$, and the eigenfunction as $f = \sum_{k=1}^{L} \beta_k \phi_k$. By choosing the test function $\eta = \phi_i (1 \leq i \leq L)$, we convert the weak form into its matrix form:

$$Q\beta = \lambda \overline{U}(\omega)\beta. \tag{6}$$

The elements of the matrix Q are defined as $Q_{ik} = \int_{\mathcal{M}} < \nabla\phi_i, \nabla\phi_k > d\mathcal{M}$. The matrix $\overline{U}(\omega)$ is a function of ω with its elements defined as $\overline{U}_{ik}(\omega) = \sum_{j=1}^{L} \omega_j U_{ijk}$, where $U_{ijk} = \int_{\mathcal{M}} \phi_i \phi_j \phi_k d\mathcal{M}$. By solving (6), we can compute the LB embedding $I_{\mathcal{M}}^{wg}$ under the new metric $\hat{g} = wg$.

2.2 Eigen-Derivatives

To realize surface deformation in the embedding space, we derive the derivatives of the eigenvalues and eigenfunctions with respect to the weight function ω.

Let λ_n and f_n denote the n-th eigenvalue and eigenfunction of the LB operator under the conformal metric ωg. We compute the derivative with respect to ω_j, the j-th component of ω, on both sides of (6) and have:

$$Q\frac{\partial f_n}{\partial \omega_j} = \frac{\partial \lambda_n}{\partial \omega_j}\overline{U} f_n + \lambda_n \frac{\partial \overline{U}}{\partial \omega_j} f_n + \lambda_n \overline{U}\frac{\partial f_n}{\partial \omega_j} \tag{7}$$

where the elements of $\frac{\partial \overline{U}}{\partial \omega_j}$ are defined as $[\frac{\partial \overline{U}}{\partial \omega_j}]_{ik} = U_{ijk}$. Pre-multiplying both sides with f_n^T, we obtain:

$$\frac{\partial \lambda_n}{\partial \omega_j} = -\lambda_n f_n^T \frac{\partial \overline{U}}{\partial \omega_j} f_n \tag{8}$$

because $f_n^T \overline{U} f_n = 1$ and $f_n^T (Q - \lambda_n \overline{U}) = 0$.

To compute the derivative of the eigenfunction, we need to solve

$$(Q - \lambda_n \overline{U})\frac{\partial f_n}{\partial \omega_j} = F_n \tag{9}$$

where $F_n = -\lambda_n f_n^T \frac{\partial \overline{U}}{\partial \omega_j} f_n \overline{U} f_n + \lambda_n \frac{\partial \overline{U}}{\partial \omega_j} f_n$. Because $Q - \lambda_n \overline{U}$ is singular, we follow [15] and write $\frac{\partial f_n}{\partial \omega_j} = \mu_{nj} + c_{nj} f_n$ with the constraint that the p-th component of u_{ij} is zero, where p is the index of the component that has the largest magnitude in f_n. This is realized by setting the p-th component of F_n as zero and the p-th row and column of $(Q - \lambda_n \overline{U})$ as zero except the diagonal term, which is set to one. Equation (9) then becomes

$$\begin{bmatrix} [Q - \lambda_n \overline{U}]_{11} & 0 & [Q - \lambda_n \overline{U}]_{12} \\ 0 & 1 & 0 \\ [Q - \lambda_n \overline{U}]_{21} & 0 & [Q - \lambda_n \overline{U}]_{22} \end{bmatrix} \mu_{nj} = \begin{bmatrix} [F_n]_1 \\ 0 \\ [F_n]_2 \end{bmatrix} \tag{10}$$

where $[F_n]_1$ is the 1 to $(p-1)$-th components of F_n, and $[F_n]_2$ is the $p+1$ to the end of the vector F_n. Assuming there is no multiplicity at λ_n [15], this problem is non-singular, and we can solve it to obtain μ_{nj}. To compute c_{nj}, we use the condition that $f_n^T \overline{U} f_n = 1$. By taking derivatives on both sides, we have $\frac{\partial f_n}{\partial \omega_j} \overline{U} f_n = 0$ and get $c_{nj} = -\mu_{nj}^T \overline{U} f_n$. This completes the solution for $\frac{\partial f_n}{\partial \omega_j}$.

3 Surface Mapping via Deformation in Embedding Space

In this section, we demonstrate the application of metric optimization by applying it to compute surface maps in the embedding space. Let $(\mathcal{M}_1, g_1)$ and $(\mathcal{M}_2, g_2)$ denote two surfaces, and ω_1 and ω_2 the weight functions on them, respectively. The eigenvalues and eigen-functions of $(\mathcal{M}_m, \omega_m g_m)(m = 1, 2)$ are denoted as $\lambda_{m,n}$ and $f_{m,n}$. To match these two surfaces in the embedding space, we minimize the following energy function with respect to the conformal metrics:

$$E(\omega_1, \omega_2) = \frac{1}{S_1}\int_{\mathcal{M}_1} d_1^2(\mathbf{x})d\mathcal{M}_1 + \frac{1}{S_2}\int_{\mathcal{M}_2} d_2^2(\mathbf{x})d\mathcal{M}_2 + \xi\sum_{i=1}^{2}\int_{\mathcal{M}_i}\|\nabla\omega_i\|^2 d\mathcal{M}_i. \quad (11)$$

The distances are defined as $d_1(x) = \min_{y\in\mathcal{M}_2}\|I_{\mathcal{M}_1}^{\omega_1 g_1}(x) - I_{\mathcal{M}_2}^{\omega_2 g_2}(y)\|_2$ and $d_2(x) = \min_{y\in\mathcal{M}_1}\|I_{\mathcal{M}_2}^{\omega_2 g_2}(x) - I_{\mathcal{M}_1}^{\omega_1 g_1}(y)\|_2$, where $I_{\mathcal{M}_1}^{\omega_1 g_1}$ and $I_{\mathcal{M}_2}^{\omega_2 g_2}$ are LB embeddings chosen to minimize the distances among all possible sign combinations [14]. The third term in the energy encourages smoothness in the weight functions and ξ is a regularization parameter.

To find the optimal metrics that minimize the energy, we iteratively update the weight functions in the gradient descent direction to deform the surfaces in the embedding space. We represent each surface as a triangular mesh $\mathcal{M}_m = (\mathcal{T}_m, \mathcal{V}_m)$ for $m = 1, 2$. For both surfaces, we use the first N eigenfunctions to approximate the embedding. At each iteration, we denote $\mathbf{u}_1(\mathcal{V}_1) = A\mathcal{V}_2$, and $\mathbf{u}_2(\mathcal{V}_2) = B\mathcal{V}_1$ as the closest point maps that minimizes d_1 and d_2 in the embedding space, where A and B are interpolation matrices. Using these two maps, we can write the energy at the current iteration in discrete form:

$$\begin{aligned} E(\omega_1, \omega_2) = \sum_{n=1}^{N}\Bigg(&\frac{1}{S_1}\Big(\frac{f_{1,n}}{\sqrt{\lambda_{1,n}}} - \frac{f_{2,n}(\mathbf{u}_1)}{\sqrt{\lambda_{2,n}}}\Big)^T U_1\Big(\frac{f_{1,n}}{\sqrt{\lambda_{1,n}}} - \frac{f_{2,n}(\mathbf{u}_1)}{\sqrt{\lambda_{2,n}}}\Big) \\ &+\frac{1}{S_2}\Big(\frac{f_{2,n}}{\sqrt{\lambda_{2,n}}} - \frac{f_{1,n}(\mathbf{u}_2)}{\sqrt{\lambda_{1,n}}}\Big)^T U_2\Big(\frac{f_{2,n}}{\sqrt{\lambda_{2,n}}} - \frac{f_{1,n}(\mathbf{u}_2)}{\sqrt{\lambda_{1,n}}}\Big)\Bigg) + \xi(\omega_1^T Q_1\omega_1 + \omega_2^T Q_2\omega_2) \end{aligned} \quad (12)$$

where U_m and Q_m are matrices defined in (6) with uniform weight, i.e., the standard metric. Using the eigen-derivatives with respect to the weight functions, we can derive the gradient flows for the weight functions as follows:

$$\begin{aligned} \frac{\partial E}{\partial\omega_1} = 2\sum_{n=1}^{N}\Bigg[&\frac{1}{S_1}\Big(\frac{1}{\sqrt{\lambda_{1,n}}}\frac{\partial f_{1,n}}{\partial\omega_1} - \frac{\partial\lambda_{1,n}}{\partial\omega_1}\frac{(f_{1,n})^T}{2\sqrt[3/2]{\lambda_{1,n}}}\Big)U_1\Big(\frac{f_{1,n}}{\sqrt{\lambda_{1,n}}} - \frac{Af_{2,n}}{\sqrt{\lambda_{2,n}}}\Big) \\ &- \frac{1}{S_2}\Big(\frac{\partial f_{1,n}}{\partial\omega_1}\frac{B^T}{\sqrt{\lambda_{1,n}}} - \frac{\partial\lambda_{1,n}}{\partial\omega_1}\frac{(Bf_{1,n})^T}{2\sqrt[3/2]{\lambda_{1,n}}}\Big)U_2\Big(\frac{f_{2,n}}{\sqrt{\lambda_{2,n}}} - \frac{Bf_{1,n}}{\sqrt{\lambda_{1,n}}}\Big)\Bigg] + 2\xi Q_1\omega_1 \end{aligned} \quad (13)$$

$$\begin{aligned} \frac{\partial E}{\partial\omega_2} = 2\sum_{n=1}^{N}\Bigg[&\frac{1}{S_2}\Big(\frac{1}{\sqrt{\lambda_{2,n}}}\frac{\partial f_{2,n}}{\partial\omega_2} - \frac{\partial\lambda_{2,n}}{\partial\omega_2}\frac{(f_{2,n})^T}{2\sqrt[3/2]{\lambda_{2,n}}}\Big)U_2\Big(\frac{f_{2,n}}{\sqrt{\lambda_{2,n}}} - \frac{Bf_{1,n}}{\sqrt{\lambda_{1,n}}}\Big) \\ &- \frac{1}{S_1}\Big(\frac{\partial f_{2,n}}{\partial\omega_2}\frac{A^T}{\sqrt{\lambda_{2,n}}} - \frac{\partial\lambda_{2,n}}{\partial\omega_2}\frac{(Af_{2,n})^T}{2\sqrt[3/2]{\lambda_{2,n}}}\Big)U_1\Big(\frac{f_{1,n}}{\sqrt{\lambda_{1,n}}} - \frac{Af_{2,n}}{\sqrt{\lambda_{2,n}}}\Big)\Bigg] + 2\xi Q_2\omega_2 \end{aligned} \quad (14)$$

Starting from a pair of embeddings $I_{\mathcal{M}_1}^{\omega_1 g_1}$ and $I_{\mathcal{M}_2}^{\omega_2 g_2}$ that achieve the minimum energy among 2^N possible sign combinations, we iteratively deform the embeddings by optimizing the metrics in the gradient descent direction following above

equations. Note that the search through 2^N combinations only needs be done once in the first iteration to resolve sign ambiguities in eigenfunctions. After that, we can resolve the sign ambiguities efficiently by comparing correlations between corresponding eigenfunctions in consecutive iterations because only small perturbations are introduced in one iteration. Once the iterative process converges, we obtain $\mathbf{u}_1$ and $\mathbf{u}_2$ as the maps between these two surfaces.

4 Experimental Results

In this section, we present experimental results on hippocampal surface mapping to demonstrate the application of our method in brain imaging research. In the first experiment, we present detailed results on the mapping of two surfaces. The robustness and clinical relevance of our method are demonstrated in the second experiment on a clinical dataset of 109 subjects. A comparison with the popular SPHARM tool is presented in the third experiment.

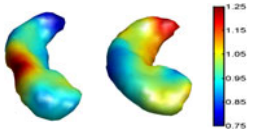

Fig. 2. The optimized weight function in the conformal metric of the two surfaces

4.1 Mapping Results of Two Surfaces

In this experiment, we apply our metric optimization method to the two surfaces in Fig. 1(a) and (d). The parameters are $N = 20$, $\xi = 0.1$ and 150 iterations of metric optimization according to equations (13) and (14) are used to obtain the final maps $\mathbf{u}_1$ and $\mathbf{u}_2$. The computational time is around 15 minutes on a PC.

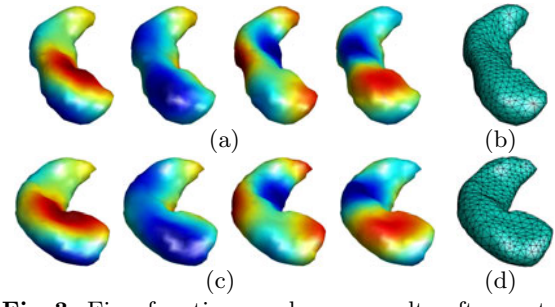

Fig. 3. Eigenfunctions and map results after metric optimization. (a) Eigenfunctions of $\mathcal{M}_1$. (b) $\mathbf{u}_2(\mathcal{M}_2)$. (c) Eigenfunctions of $\mathcal{M}_2$. (d) $\mathbf{u}_1(\mathcal{M}_1)$.

The optimized weight functions of these two surfaces are shown in Fig. 2, where corresponding regions exhibit complimentary metric deformations to account for non-isometric differences of these parts. Under the conformal metrics, the corresponding eigenfunctions of the two surfaces are shown in Fig. 3(a) and (c). We can see they are almost identical and agree much better than the ones in Fig. 1. The quality of the maps can be visualized by the mesh quality of $\mathbf{u}_1(\mathcal{M}_1)$ and $\mathbf{u}_2(\mathcal{M}_2)$ in Fig. 3(b) and (d). Compared with the meshes in Fig. 1(c) and (f), we can see the mesh structures are much more uniform.

4.2 Hippocampal Mapping in MS Patients with Depression

In this experiment, we demonstrate the robustness of our method by applying it to a clinical study of hippocampal atrophy in MS patients with depression. Using the Center for Epidemiologic Studies-Depression (CES-D) scale as

the measure for depression, the 109 female subjects in this study are split into two groups: low depression (CES-D$\leq$ 20) and high depression (CES-D$>$ 20). To study group differences, the right hippocampi are mapped with our metric optimization method to an atlas surface, which is the right hippocampus of one randomly selected subject. Using the computed maps, we project the mesh structure of the atlas onto all hippocampal surfaces to establish one-to-one correspondences across subjects. At each corresponding triangle of the 109 surfaces, a one-sided t-test is applied using a thickness measure [10] to test the hypothesis that MS patients with high depression have more severe hippocampal atrophy.

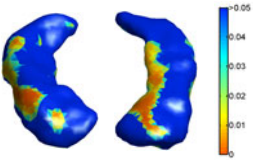

Fig. 4. Top (left) and bottom (right) views of the thickness p-value map from our method

As shown in the significance map of p-values in Fig. 4, the highlighted regions indicate larger atrophy occurs in the right hippocampus of MS patients with high depression. To correct for multiple comparisons, we applied 1000 permutation tests and an overall p-value of 0.017 is obtained, which means the overall significance of the thickness map. To further validate the clinical relevance of the thickness map, we test the correlation of the thickness measure and CES-D scores at each triangle. The correlation coefficients are plotted in Fig. 5(a) with the significance map of the correlation in Fig. 5(b), which indicates highlighted regions in Fig. 4 match excellently to regions with significant negative correlations between thickness and CES-D scores. This shows that patients with more severe depressive symptoms in deed have more hippocampal atrophy in the highlighted regions detected by our method.

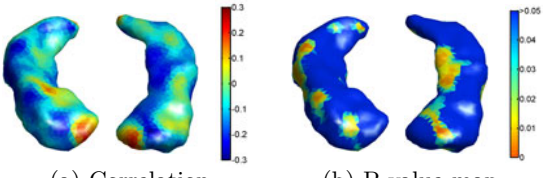

(a) Correlation. (b) P-value map.

Fig. 5. The correlation between CESD and thickness, and its p-value map

4.3 Comparison with SPHARM

In this experiment, we apply the popular SPHARM tool to map the same group of hippocampal surfaces in the second experiment. We adopt the suggested parameters for hippocampus in the manual of SPHARM [5]. Using the correspondences established by the SPHARM maps, the same one-sided t-tests are applied at each triangle to test for group differences among the 109 surfaces. The resulting significance map of p-values is plotted in Fig. 6. To correct for multiple comparisons, we also apply 1000 permutation tests and the overall p-value is 0.07. By comparing the results in Fig. 4, 5 and 6, we can see that our method achieves better performance by detecting more group differences that correlate well with clinical variables.

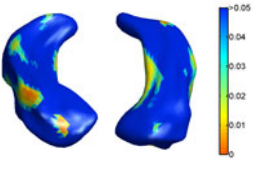

Fig. 6. Top (left) and bottom (right) views of the thickness p-value map from the SPHARM tool

5 Conclusions

In this work we proposed a general approach for surface deformation in LB embedding space by optimizing conformal metrics on surfaces. In future work, we will minimize bias in statistical analysis by developing group-based techniques. We will also conduct more extensive comparisons with existing methods.

References

1. Thompson, P., Hayashi, K., de Zubicaray, G., Janke, A., Rose, S., Semple, J., Hong, M., Herman, D., Gravano, D., Doddrell, D., Toga, A.: Mapping hippocampal and ventricular change in Alzheimer disease. NeuroImage 22(4), 1754–1766 (2004)
2. Joshi, S., Miller, M.: Landmark matching via large deformation diffeomorphisms. IEEE Trans. Imag. Process. 9(8), 1357–1370 (2000)
3. Davies, R., Twining, C., Allen, P., Cootes, T., Taylor, C.: Shape discrimination in the hippocampus using an MDL model. In: Taylor, C.J., Noble, J.A. (eds.) IPMI 2003. LNCS, vol. 2732, pp. 38–50. Springer, Heidelberg (2003)
4. Yeo, B., Sabuncu, M., Vercauteren, T., Ayache, N., Fischl, B., Golland, P.: Spherical demons: Fast surface registration. In: Metaxas, D., Axel, L., Fichtinger, G., Székely, G. (eds.) MICCAI 2008, Part I. LNCS, vol. 5241, pp. 745–753. Springer, Heidelberg (2008)
5. Styner, M., Oguz, I., Xu, S., Brechbühler, C., Pantazis, D., Levitt, J., Shenton, M., Gerig, G.: Framework for the statistical shape analysis of brain structures using SPHARM-PDM. The Insight Journal (2006)
6. Yushkevich, P., Zhang, H., Gee, J.: Continuous medial representation for anatomical structures. IEEE Trans. Med. Imag. 25(12), 1547–1564 (2006)
7. Reuter, M., Wolter, F., Peinecke, N.: Laplace-Beltrami spectra as Shape-DNA of surfaces and solids. In: Computer-Aided Design, vol. 38, pp. 342–366 (2006)
8. Qiu, A., Bitouk, D., Miller, M.: Smooth functional and structural maps on the neocortex via orthonormal bases of the Laplace-Beltrami operator. IEEE Trans. Med. Imag. 25(10), 1296–1306 (2006)
9. Shi, Y., Lai, R., Krishna, S., Sicotte, N., Dinov, I., Toga, A.: Anisotropic Laplace-Beltrami eigenmaps: Bridging Reeb graphs and skeletons. In: Proc. MMBIA, pp. 1–7 (2008)
10. Shi, Y., Morra, J., Thompson, P., Toga, A.: Inverse-consistent surface mapping with Laplace-Beltrami eigen-features. In: Prince, J.L., Pham, D.L., Myers, K.J. (eds.) IPMI 2009. LNCS, vol. 5636, pp. 467–478. Springer, Heidelberg (2009)
11. Seo, S., Chung, M., Vorperian, H.: Heat kernel smoothing using Laplace-Beltrami eigenfunctions. In: Jiang, T., Navab, N., Pluim, J.P.W., Viergever, M.A. (eds.) MICCAI 2010. LNCS, vol. 6363, pp. 505–512. Springer, Heidelberg (2010)
12. Reuter, M.: Hierarchical shape segmentation and registration via topological features of Laplace-Beltrami eigenfunctions. Int'l Journal of Computer Vision 89(2-3), 287–308 (2010)
13. Rustamov, R.M.: Laplace-beltrami eigenfunctions for deformation invariant shape representation. In: Proc. Eurograph. Symp. on Geo. Process. pp. 225–233 (2007)
14. Lai, R., Shi, Y., Scheibel, K., Fears, S., Woods, R., Toga, A., Chan, T.: Metric-induced optimal embedding for intrinsic 3D shape analysis. In: Proc. CVPR, pp. 2871–2878 (2010)
15. Nelson, R.: Simplified calculation of eigenvector derivatives. AIAA Journal 14(9), 1201–1205 (1976)